Research Article

# Modular Micro-Physiological Human Tumor/Tissue Models Based on Decellularized Tissue for Improved Preclinical Testing

*Johanna Kühnemundt[1,#], Heidi Leifeld[1,#], Florian Scherg[1,#], Matthias Schmitt[1,#], Lena C. Nelke[1], Tina Schmitt[1], Florentin Baur[1,2], Claudia Göttlich[1,2], Maximilian Fuchs[3], Meik Kunz[3,4], Matthias Peindl[1], Caroline Brähler[1], Corinna Kronenthaler[1], Jörg Wischhusen[5], Martina Prelog[6], Heike Walles[1,2,7], Thomas Dandekar[3], Gudrun Dandekar[1,2,§] and Sarah L. Nietzer[1,2,§]*

[1]Department Tissue Engineering and Regenerative Medicine, University Hospital Würzburg, Würzburg, Germany; [2]Translational Center Regenerative Therapies, Fraunhofer Institute for Silicate Research ISC, Würzburg, Germany; [3]Bioinformatics, Biocenter, University of Würzburg, Würzburg, Germany; [4]Chair of Medical Informatics, Friedrich-Alexander University (FAU) of Erlangen-Nürnberg, Erlangen, Germany; [5]University Hospital Würzburg, Department for Obstetrics & Gynecology, Section for Experimental Tumor Immunology, University of Würzburg, Würzburg, Germany; [6]Children's University Hospital, Pediatric Rheumatology/Special Immunology, University of Würzburg, Würzburg, Germany; [7]FVST, Core Facility Tissue Engineering, Otto-von Guericke University, Magdeburg, Germany

**Abstract**

High attrition rates associated with drug testing in 2D cell culture and animal models stress the need for improved modeling of human tumor tissues. In previous studies, our 3D models on a decellularized tissue matrix have shown better predictivity and higher chemoresistance. A single porcine intestine yields material for 150 3D models of breast, lung, colorectal cancer (CRC) or leukemia. The uniquely preserved structure of the basement membrane enables physiological anchorage of endothelial cells and epithelial-derived carcinoma cells. The matrix provides different niches for cell growth: on top as monolayer, in crypts as aggregates, and within deeper layers. Dynamic culture in bioreactors enhances cell growth. Comparing gene expression between 2D and 3D cultures, we observed changes related to proliferation, apoptosis and stemness. For drug target predictions, we utilize tumor-specific sequencing data in our *in silico* model, finding an additive effect of metformin and gefitinib treatment for lung cancer *in silico*, validated *in vitro*. To analyze mode-of-action, immune therapies such as trispecific T-cell engagers in leukemia or toxicity on non-cancer cells, the model can be modularly enriched with human endothelial cells (hECs), immune cells and fibroblasts. Upon addition of hECs, transmigration of immune cells through the endothelial barrier can be investigated. In an allogenic CRC model, we observe a lower basic apoptosis rate after applying PBMCs in 3D compared to 2D, which offers new options to mirror antigen-specific immunotherapies *in vitro*. In conclusion, we present modular human 3D tumor models with tissue-like features for preclinical testing to reduce animal experiments.

## 1 Introduction

### 1.1 Preclinical test systems in oncology

Preclinical models in oncology still rely mostly on two-dimensional (2D) culture and on animal experiments. Translatability of such results into the clinic is, however, limited (Bhattacharjee, 2012). About 30% of failures in cancer-related drug testing are related to safety and toxicity issues. In addition, more than 50% of preclinical models fail to predict efficacy in patients. The need for improvements in this area is thus obvious (Arrowsmith and Miller, 2013). Improved *in vitro* models could drastically reduce the number of animals used for basic, preclinical as well as translational research. Of a total of about 9.6 million animals used in basic (45%) and translational/applied research (23%) in the EU in 2017, cancer was the third-leading or even the most common field of application, respectively (EC, 2020).

[#] contributed equally; [§] shared senior authors

Received August 14, 2020; Accepted December 9, 2020;
Epub December 11, 2020; © The Authors, 2021.

**ALTEX 38(2), 289-306.** doi:10.14573/altex.2008141

Correspondence: Sarah L. Nietzer, PhD
Department Tissue Engineering and Regenerative Medicine
University Hospital Würzburg
Röntgenring 11, 97070 Würzburg, Germany
(sarah.nietzer@uni-wuerzburg.de)

Innovative three-dimensional (3D) approaches reflecting relevant aspects of the *in vivo* situation reach from transwell cultures, spheroids, synthetic or biological matrices, 3D printed models and organoids to whole organ-on-a-chip models (Albritton and Miller, 2017; Katt et al., 2016; Nath and Devi, 2016; Santo et al., 2017; van Duinen et al., 2015; Weeber et al., 2017; Xu et al., 2014). As so far no "magic bullet" exists for all cancer types, stages and patients, no single test system can be expected to meet the testing requirements of all different therapeutic approaches. Depending on the respective questions and the therapeutic strategies to be assessed, the required test systems have to be specifically adapted. More advanced therapeutic options, including targeted and immune therapies and their combinations with more conventional chemotherapeutics or radiation approaches, require suitable complex models. Optimized *in vitro* models could also reduce the large number of animals required to analyze different combinations of compounds.

There are, however, defined features that are commonly advantageous for reliable models. A fully human setting avoids extrapolations across species boundaries. A gradual 3D growth of cancer cells is more likely to result in structures similar to those found in tumors *in vivo*. Due to their unphysiologically high proliferation index (often 80 to 90%), 2D models generally lead to an overestimation of cytostatic effects (Cree et al., 2010). General tissue architecture, which includes response-modulating accessory cells as found in the tumor microenvironment, can only be replicated in complex 3D models. Moreover, a loss of tumor stroma over time, which is frequently observed in transplantable *in vivo* tumor models as well as in organoids (Yada et al., 2018; Kim et al., 2019), may render these test systems insensitive to important contributions from the stromal compartment. Serious limitations also apply for the testing of immunotherapeutic agents in humanized animal models: Apart from the enormous cost and effort, species-specific differences of cytokines typically result in an impaired maturation and differentiation of certain human immune cell subsets in a murine microenvironment (Rongvaux et al., 2013, 2014; Song et al., 2019; Walsh et al., 2017; Anselmi et al., 2020).

Being able to monitor immune-mediated tumor control in a predictive, fully human *in vitro* system will thus significantly advance preclinical research.

### 1.2 3D tumor tissue models

The present study aims to establish high-output modular 3D tissue drug test systems that model tissue niches sufficiently well to enable a reliable testing of drug responses. While investigations of homophilic cell-cell-interactions, cell migration, invasion, and changes of signaling pathways may also yield reasonably reliable results in 2D tumor cell culture models, interactions of tumor cells with different other cell types such as fibroblasts, hECs and immune cells are challenging to explore in such 2D systems.

In this study we present modular human 3D tumor models for lung, colorectal, and breast cancer as well as leukemia. Their complexity can be adapted according to the therapeutic question. All models are based on the patented BioVaSc-TERM® (Biological Vascularized Scaffold – Tissue Engineering Regenerative Medicine (Jannasch et al., 2015; Linke et al., 2007; Schanz et al., 2010) (Ref, DE 30 2014 008, Int.: 1 255 634, US: 79168704)), which is derived from an intestinal porcine tissue matrix. When seeded with tumor cells, it is referred to as OncoVaSc-TERM®. The BioVaSc-TERM®-technology and its derivatives are already being used for vascularized skin equivalents as well as for intestinal and airway models (Groeber et al., 2016; Schweinlin et al., 2017). As the decellularized and sterilized intestine of one single pig is sufficient to generate about 150 3D tumor models, the approach minimizes the use of animals for research.

The extremely versatile biological matrix "Small Intestinal Submucosa with mucosa" (SISmuc) is produced by removing all vessel structures and offers different tissue niches: i) on the surface of villi, ii) within former crypts, and iii) within deeper layers of the collagen matrix. As a unique feature of the matrix, structures of the basement membrane are preserved after decellularization, which enables physiological anchorage-dependent growth of epithelial cells (Stratmann et al., 2014). Furthermore, this structure enables the testing of substances that are intended to eliminate invasive tumor cells once they cross this natural border. Early steps in metastasis formation can also be studied in order to understand underlying mechanisms and to identify possible points of action. Our matrix-based lung cancer models were already shown to accurately reflect drug responses upon targeted therapies observed in the clinic – not just better than 2D, but partly also more reliably than animal models (Göttlich et al., 2018; Stratmann et al., 2014).

### 1.3 Applications of 3D tumor tissue models

Building on these previous findings, we now characterized our modular micro-physiological 3D tissue models using microarrays and immunohistochemical staining for stem cell markers to analyze differences between 2D and 3D conditions in more detail. Supported by *in silico* analyses, our 3D test system offers a time-efficient way to test effects of drug combinations on complex tissues, to analyze effects on signaling pathways, and to identify interdependencies. As an example, we present a new combination therapy for lung cancer treatment combining metformin and gefitinib. Our 3D tissue culture test system not only validates the prediction. It also allows functional tests to identify requirements for a synergistic response.

The modular approach further enables the addition of hECs to 3D tissue models. These hECs were seeded onto the former serosal side of the decellularized intestine so that toxic effects on the vasculature and the diapedesis behavior of immune cells can be addressed. To include the stromal compartment, we established different co-culture models with primary fibroblasts and found that dynamic cell culture within flow bioreactors overcomes problems with poor stroma development *in vitro* (Nietzer et al., 2016). In the context of immune therapeutic approaches, we observed an enhanced efficacy compared to 2D culture of MHCI independently acting trispecific T-cell engagers in a 3D leukemia model with artificial endothelium. Moreover, CRC 3D models show a drastically reduced induction of tumor cell apoptosis by allogeneic peripheral blood mononuclear cells (PBMCs) in monocultures and also in fibroblast-enriched co-culture mod-

els. This indicates that complex 3D models with allogeneic cells offer a therapeutic window for testing antigen-independent immune-stimulatory or -inhibitory agents.

These promising advantages of our modular 3D culture approach should reduce attrition rates and save animal experiments on account of its more physiologic tissue features, which are examined in detail in the following.

## 2 Animals, materials and methods

*Animals*

The matrices SISmuc and SISser (used for the leukemia model with an endothelial barrier) were prepared from porcine jejunal segments of young pigs (German landrace, local supplier). The animals used for organ removal were not bred specifically for research purposes but obtained from a local supplier who breeds animals for food production. SISmuc consists of small intestine submucosa (SIS) and mucosa (muc). SISser consists of SIS and serosa (ser). All explantations were in compliance with the German Animal Protection Laws (§4 Abs. 3), and all animals received humane care in compliance with the guidelines of the FELASA, WHO and FDA (WHO-TRS978 Annex3 und FDA-OCTGT Preclinical Guidance) after approval by our institutional animal protection board (registration reference number #2532-2-12, Ethics Committee of the District of Unterfranken, Würzburg, Germany). Pigs were anesthetized and then euthanized prior to surgery, therefore not suffering from pain or distress. To keep the number of sacrificed animals low, many different organs were removed for various research projects.

*Matrix preparation*

Chemical decellularization of jejunal segments was performed according to standardized protocols (Jannasch et al., 2015; Linke et al., 2007; Schanz et al., 2010). The jejunum was explanted, rinsed and chemically decellularized with a sodium deoxycholate monohydrate solution. Afterwards the vascular tree was manually removed, and the product was sterilized (γ-sterilization).

*Primary cells and cell lines*

Primary human cells were obtained with informed consent according to ethical approval granted by the Institutional Ethics Committee of the University Hospital Würzburg (approval number 182/10).

All cells were cultured under standard culture conditions (37°C, 5% $CO_2$). We used HROC24 and HROC87 cells (kindly provided by Dr Michael Linnebacher, University Hospital Rostock) (Mullins et al., 2019) cultured in DMEM/F12 medium with GlutaMAX™ (Gibco/Life Technologies, USA) supplemented with 10% FCS. HCC827, MCF7 (both purchased from DSMZ), MDA-MB-231 cells (purchased from ATCC), THP-1 (purchased from DSMZ) and SW480 (purchased from DSMZ) were cultured in RPMI 1640 medium with GlutaMAX™ (Gibco/Life Technologies, USA) supplemented with 10% FCS, except for HCC827 cells, which were cultured with 20% FCS. Human dermal fibroblasts were isolated from the dermis of foreskin biopsies and cultured in DMEM with GlutaMAX™ (Gibco/Life Technologies, USA) supplemented with 10% FCS and 100 mM sodium pyruvate. Primary microvascular hECs were isolated from the dermis of foreskin biopsies and cultured in VascuLife Media (Lifeline Cell Technology, USA). Endothelial cell cultures were morphologically confirmed to contain no fibroblasts after isolation from a skin biopsy. If fibroblasts were found in the cultures, cells were sorted using magnetic associated cell sorting beads directed against the endothelial marker CD31 (Miltenyi, Germany). Fibroblasts and hECs were cultured in the presence of 1% penicillin/streptomycin (P/S) after isolation until the first passaging was performed. PBMC for trispecific antibody treatment (delivered by PD G. Stuhler, HLA-A2 negative, CMV positive) were frozen at -80°C and thawed overnight prior to use in RPMI with 10% FCS and 1% P/S. PBMC were generated from buffy coats via Ficoll gradient isolation and cultured in RPMI 1640 medium with GlutaMAX™ (Gibco/Life Technologies, USA) with 10% FCS.

We applied the culture conditions recommended by the supplier to the respective cell lines and used the lowest quantity of FCS that is feasible for the different cell types to reduce FCS consumption. So far, the used cells did not grow with defined FCS-free media. In case of co-culture models, equal parts of cell-specific media were mixed. Cell lines were used in passages up to 20, while primary cells were only used until passage 6. Tumor cell lines were passaged twice a week, and medium was changed every 2 to 3 days. Cells were checked for mycoplasma contaminations every 8 to 10 weeks by PCR (Minerva Biolabs, Germany).

*Preparation of tumor models*

Single pieces of SISmuc or SISser matrix were fixed between two metal rings (cell crowns) and seeded with 100,000 tumor cells on the mucosal side or with 300,000 hECs on the submucosal side. To create a tight endothelial barrier, hECs were seeded 3 to 5 days prior to seeding with tumor cells. Tumor models were placed in 12-well plates with 1 mL medium in the inner compartment and 1.5 mL in the outer compartment of the cell crown. For static cell culture, the models were cultured for 11 days before treatment with the test substance. During static cell culture, medium was changed every 2 to 3 days. For dynamic culture, the models were placed in bioreactor chambers after 3 days of static pre-culture. The customized bioreactors used, described in (Nietzer et al., 2016), were connected to a peristaltic pump and a medium reservoir containing 45 mL cell-specific medium. The pump ensured a constant medium flow of 3-4 mL/min, avoiding additional sheer stress to the cells. After 14 days of dynamic culture, the models were treated for 3-5 days with the test substance. During dynamic cell culture, medium was changed every 7 days. All test substances were administered via the cell culture medium.

*Treatment of cells in 2D and 3D*

For 2D cell culture, cells were cultured in 12-well plates. Tipifarnib (Selleck Chemicals, USA) in DMSO was applied in different concentrations to the cell culture medium for 5 days with a medium change on the third day. For 3D cell culture, hECs were seeded on SISser and cultured for 14 days prior to adding THP-

1 cells to the medium on day 14, with or without tipifarnib, and cultured for the next 5 days (with a complete medium change on day 17). In case of the trispecific antibody treatment (AB1: VLαCD3-scFvαHLA-A2; AB2: VHαCD3-scFvαCD45; antibodies provided by PD G. Stuhler), antibody 1 and/or 2 (each 30 nM) and 200,000 PBMC as apoptosis inductors in THP-1 cells via trispecific antibodies were added to 200,000 THP-1 cells in each well of the 12-well plate (in Vasculife® medium with 1% P/S) and incubated for 24 h. The setting in the 3D model was the same as in the 2D model with the difference that, where indicated, the cell + DMSO/trispecific antibodies mixture was added to each cell crown onto the surface of the 3D endothelial monolayer. Treatment with 10 mM metformin (Merck, Germany) and 1 µM gefitinib (Absource Diagnostics, Germany) of 3D models started on day 11 for 3 days until day 14 of 3D cell culture.

*Flow cytometry*
Cells in the supernatant were resuspended and transferred to a reaction tube. For cell death quantification, cells were centrifuged (4°C, 300 x g, 5 min) and washed in sterile PBS with 0.5% BSA. Cells were resuspended in 500 µL PBS with 0.5% BSA, and 5 µL 7-aminoactinomycin D (7-AAD) (Biozol, Germany) was added per sample. 7-AAD intercalates into the DNA and is used to distinguish apoptotic cells (7-AAD+) from viable cells (7-AAD-). After incubation in the dark on ice for 10 min, FACS measurements were performed (FACSCalibur, BD, Germany). Data analysis was performed with the software FlowJo 6.0. For treatment with trispecific antibodies, we confirmed that the primary hECs we used for the model reacted with the anti-HLA-A2 antibody (BD Pharmingen, Germany) in flow cytometry prior to reseeding the scaffold.

*TUNEL Assay*
To detect DNA damage in hECs, the *in situ* Cell Death Detection Kit, POD (Roche, Switzerland) was used according to the manufacturer's instructions. Staining was visualized using a BZ-9000 microscope (Keyence, Japan).

*Apoptosis measurements using M30 ELISA*
For quantification of epithelial apoptosis, the M30 CytoDeath™ (PEVIVA®, TECOmedical, Germany) assay was used to measure the caspase 9-cleaved product of cytokeratin 18 in the cell culture supernatant every 24 h during treatment. This neo-epitope is specifically expressed by apoptotic epithelial cells. The M30 CytoDeath™ assay was performed according to the manufacturer's protocol. Supernatants of static cell cultures were obtained from the inside of the cell crowns. Supernatants of dynamic cell cultures were obtained via a sampling port integrated into the tubing of a flow bioreactor.

*Quantification of proliferation*
Ki-67 staining was quantified as follows: At least 6 images of each sample were taken with a fluorescence microscope (BZ-9000, Keyence, Japan). DAPI was counted automatically using the software BZ Analyzer (Keyence, Japan) to determine the total cell number. Ki-67-positive cells were counted manually. For each image, the number of Ki-67-positive cells in percent of total cell number was calculated, and the mean of each sample was used for statistical analysis.

*Statistical analysis*
All pairwise comparisons were assessed using a Student's t-test for unpaired samples. Results were corrected for multiple testing using Bonferroni's adjustment. P values $< 0.05$ were considered significant. Presentation of the flow cytometry data in the coordinate system was realized by SigmaPlot Version 10.0 (Systat Software, Inc.). M30 and Ki-67 quantifications were analyzed and presented with R[1].

*Histological and immunohistochemical staining*
As an endpoint measurement, the tumor models were fixed in a 4% paraformaldehyde solution for 2 h, embedded in paraffin, and cut in a microtome at 3-5 µm. Hematoxylin and eosin (H&E) staining (Morphisto, Germany) was performed according to the manufacturer's protocol. Non-immunofluorescent immunohistochemical staining was performed using the 3,3'-diaminobenzidine (DAB) system (DCS Innovative Diagnostik-Systeme, Germany) according to the manufacturer's protocol. Here, DAB is oxidized in the presence of a horseradish-peroxidase and hydrogen peroxide, resulting in the formation of a brown dye at areas of antibody binding.

The following primary antibodies were used: rabbit anti-CD44 (Abcam, Cat# ab51037, RRID: AB_868936), mouse anti-CD133 (R&D systems, Cat# MAB 4399 RRID: AB_2100194), mouse anti-CD166 (Abcam, Cat# ab49496, RRID: AB_868825), mouse anti-EpCAM (Abcam, Cat# ab8601, RRID:AB_306663). For immunofluorescent staining, primary antibodies were used against Col IV (Abcam Cat# ab6586, RRID: AB_305584), vimentin (Abcam Cat# ab92547, RRID: AB_10562134), Ki-67 (Abcam Cat# ab16667, RRID: AB_302459), CD45 (Dako Cat# M0701, RRID: AB_2314143) and pan-cytokeratin (Sigma-Aldrich Cat# C2562, RRID: AB_476839; this antibody was the only one derived from ascites fluid).

Primary antibodies were diluted 1:100 in antibody diluent (DCS Innovative Diagnostik-Systeme, Germany) and incubated over night at 4°C. As secondary antibodies, donkey anti-mouse IgG (Thermo Fisher Scientific Cat# A-31571, RRID: AB_162542) conjugated to Alexa-647 or donkey anti-rabbit IgG (Thermo Fisher Scientific Cat# A-31572, RRID: AB_162543) conjugated to Alexa-555 were diluted 1:400 in antibody diluent and incubated for 1 hour at room temperature (RT). Cell nuclei were counterstained using 4′,6-diamidino-2-phenylindole (DAPI), which binds to DNA. DAPI was diluted in the embedding medium Fluoromount-G (Thermofisher Scientific, USA). Images were taken using a digital microscope (BZ-9000, Keyence, Japan).

[1] https://cran.r-project.org/

*Ultrastructural analysis*
Samples were washed with pre-warmed PBS with calcium and magnesium, and cell-free edges were removed with a scalpel prior to fixation in a 6.25% or 2.5% solution of glutaraldehyde overnight at 4°C. Further sample preparation was performed at the Imaging Core Facility, Biocenter, University of Würzburg. For ultrastructural analysis of the unseeded scaffold as well as the 3D tumor models, scanning (SEM) electron microscopy images were also taken at the Imaging Core Facility, Biocenter, University of Würzburg. To analyze changes in scaffold structure after cell culture, the tumor models were decellularized after 14 days of cell culture. To this aim, the samples were incubated twice in sodium deoxycholate (1 h at RT), washed twice for 10 min in PBS, incubated in DNase I solution for 2 h at 37°C and rinsed in PBS prior to fixation.

*Microarray data*
For RNA isolation with the RNeasy Micro Kit (Qiagen, Germany) from cells in 3D experiments, frozen SISmuc stored at -80°C was used. Isolation was carried out according to the manufacturer's protocol. While still frozen, tissue was cut into small pieces with a scalpel and transferred into 350 µL Buffer RLT in a 2 mL reaction tube. Heat-sterilized steel beads were added to the tubes, and the tissue was lysed at 50 Hz for 5 min with a tissue lyser device. Samples were centrifuged at full speed for 3 min, and supernatants were transferred to a new 1.5 mL tube. One volume of RNAse-free 70% ethanol was added, and samples were mixed by pipetting. Following transfer, complete contents were centrifuged in RNeasy MinElute spin columns for 15 s at 8,000 x g. Further steps were carried out according to the manufacturer's protocol.

Isolation of RNA from cells from 2D experiments was done according to the RNeasy Mini Kit protocol. RNA concentrations were determined by absorbance measurements at 260 and 280 nm using the NanoQuant Plate for the Infinite M200 plate reader (Tecan, Switzerland). Quality control of RNA samples using the Agilent 2100 Bioanalyzer and related reagents as well as all microarray experiments and data analysis were performed by Claus-Jürgen Scholz and colleagues from the Core Unit Systems Medicine at the Interdisciplinary Centre for Clinical Research (IZKF), University of Würzburg. In brief, 100 ng of RNA was first reverse-transcribed to cDNA, before cDNA was re-transcribed into labeled cRNA using the Affymetrix IVT Plus Kit. Subsequently, 130 µL hybridization mix prepared from labeled cRNA fragments was hybridized for 16 h at 45°C and 60 rpm to GeneChip PrimeView arrays. Microarrays were washed and stained in the Affymetrix Fluidics Station 450. Microarrays were scanned using a GeneChip Scanner 3000 7G (Affymetrix, USA). The data were deposited with GEO database under accession number GSE79078.

*Bioinformatics and* in silico *modeling*
*Module 3D tissue simulations:* Signaling network reconstruction was based on available literature and on biochemical and human interactome database sources such as KEGG and IMEx. To model individual drug actions as well as effects of combinations, dynamic simulations of cellular pathways also considered known impacts of different drugs. For data-driven modeling, signaling network reconstruction was combined with dynamic simulations of cellular pathways: First, the network topology was created and edited in CellDesigner (version 3.5.1) (Matsuoka et al., 2014) and exported as xml-file. Importantly, the Boolean logic of the network was considered, i.e., activating and inhibitory interactions between receptors, proteins and protein cascades. Modifying crosstalk was also implemented. Next, dynamic simulations were conducted applying the SQUAD tool (Di Cara et al., 2007). SQUAD reads the topology of the network using the xml file generated from CellDesigner. The ON- and OFF-states of the network were also considered for dynamic modeling. SQUAD automatically interpolates between the different network states using exponential functions. To model signal propagation in the network, SQUAD further considers the Boolean network topology, concatenating the exponential functions accordingly. The trajectories of full or partial activation down to no inhibition were calculated for the whole network and for all included proteins. Different mutational profiles and treatment were integrated into the dynamic simulation via the SQUAD perturbation function. Protocols were saved in prt file format. Outcomes were assessed by readouts proliferation and apoptosis as basic markers and considering all available data (in particular phosphorylation status of involved proteins and protein cascades).

*Module omics data analysis:* Data from microarray experiments was preprocessed in the R v3.2.1 environment with Bioconductor packages affy and vsn; VSN normalization and RMA probeset summary were performed with the vsnrma command using default parameter settings. Fold change values of treated (test dataset) vs untreated (reference dataset) were calculated and log2-transformed for 2D and 3D samples individually. Cut-off values for significance were set to ± 1.0 log2 fold change. Gene transcripts that showed differential expression upon treatment in HCC827 but not in A549 cells were selected for further analysis. Differentially expressed genes (DEGS) that showed up- or downregulation in HCC827 in 3D but not in 2D in response to gefitinib were clustered into gene lists, respectively. The functional enrichment analysis using the DEGS was performed using g:Profiler web tool (Raudvere et al., 2019), and relevant enriched terms (adj. p value < 0.05) were shown as table and plotted using ggplot2 package version 3.3.2 (Wickham, 2009) in R version 4.0.2 (according to (Fuchs et al., 2020)).

## 3 Results

### 3.1 Generation of micro-physiological human tumor models on a porcine tissue matrix

In order to generate human tumor models representing the *in vivo* situation more closely than 2D cell cultures or simple spheroids, we used pieces of the porcine intestinal jejunum deriving from the BioVaSc-TERM®. These comprise an intestinal loop (Fig. 1A) with an arterial entrance (red arrow) and a venous outward flow (blue arrow) and enable reseeding of the whole vascular tree with hECs. For the 3D tumor tissue models, only the former gut wall without the vessel system is used after decellularization. The porcine matrix consists of three different main

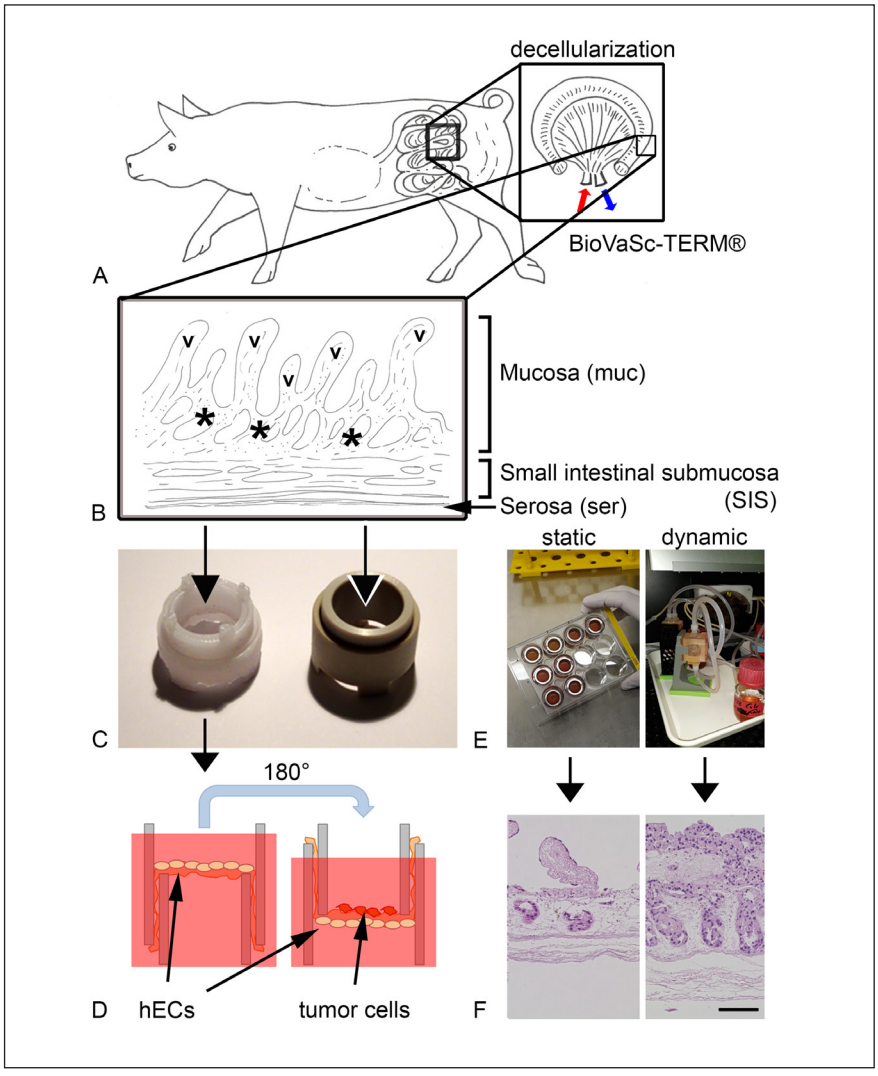


**Fig. 1: Generation of 3D tumor models by seeding a decellularized porcine jejunum with tumor cells**
(A) The collagen-rich matrix derived from porcine jejunum as a "Biological Vascularized Scaffold for Tissue Engineering and Regenerative Medicine" (BioVaSc-TERM®). (B) The wall of the former gut consists of extracellular matrix (ECM) components and maintains the tissue architecture of the intestine with villi (v) and crypt structures (*). Different layers are preserved: mucosa, small intestinal submucosa and serosa. Two different matrices can be prepared: (i) the SISmuc consists of the former small intestinal submucosa (SIS) and the mucosa (muc), while (ii) the SISser consists of the former SIS and the serosa (ser). (C) The matrix is fixed within two cell crowns, designed for seeding with cells either on both sides of the matrix (right, white crown in C) or for seeding with cells only on one side of the matrix (left, in brown). (D) Different cell types like human endothelial cells (hECs) and tumor cells can be seeded on the matrix. (E) Generated matrix-inserts can be placed in 12-well plates similar to transwells or in custom-made bioreactors for dynamic culture. (F) Cells (blue in the H&E staining) can be seeded on the surface of the collagen matrix, and cell growth is enhanced in bioreactor cultures. Scale bar in F (bottom right): 100 µm.

layers (Fig. 1B): (i) the mucosa, (ii) the small intestinal submucosa (SIS) and (iii) the serosa. Subsequently, two different tissue matrices can be derived: the SISmuc is composed of the former SIS and the mucosa, while the SISser contains the former SIS and the serosa. As a unique feature, structures of the basement membrane are preserved on top of the mucosa after the chemical decellularization process.

Both matrices can be fixed between two cell crowns, resulting in inserts for 12-well plates similar to a transwell system (Fig. 1C,D,E). They can also be fixed in flow bioreactors for dynamic cell culture (Fig. 1E). Different designs of cell crowns are possible: either they can be used upside down for two-sided cell culture (white cell crown in Fig. 1C) or upright for one-sided cell culture (brown cell crown in Fig. 1C). Dynamic culture in bioreactors enhances cell growth on the matrix (blue in Fig. 1F) compared to static cell culture (Fig. 1F).

Cells grown in static cell culture reach a state similar to tissue homeostasis after about 11 days of culture. In the absence of major changes in proliferation and apoptosis, cells can then be used for drug tests over a period of approximately 7 days (Fig. S1[2]). While dynamic models in bioreactors have a lower through-put, they benefit from better nutrient supply and waste disposal via the medium flow, thus mimicking *in vivo* conditions more closely. As dynamic culture improves cell growth and maintenance, the duration of drug application can be extended for up to several weeks.

### 3.2 The tissue matrix

After the decellularization process as described before (Jannasch et al., 2015; Linke et al., 2007; Schanz et al., 2010), the main part of the SISmuc matrix is composed of collagen fibers covered with the structurally preserved basal lamina on the mucosal side of the matrix (Fig. 2A). The villi structures are intact (Fig. 2B). With-

[2] doi.10.14573/altex.2008141s1

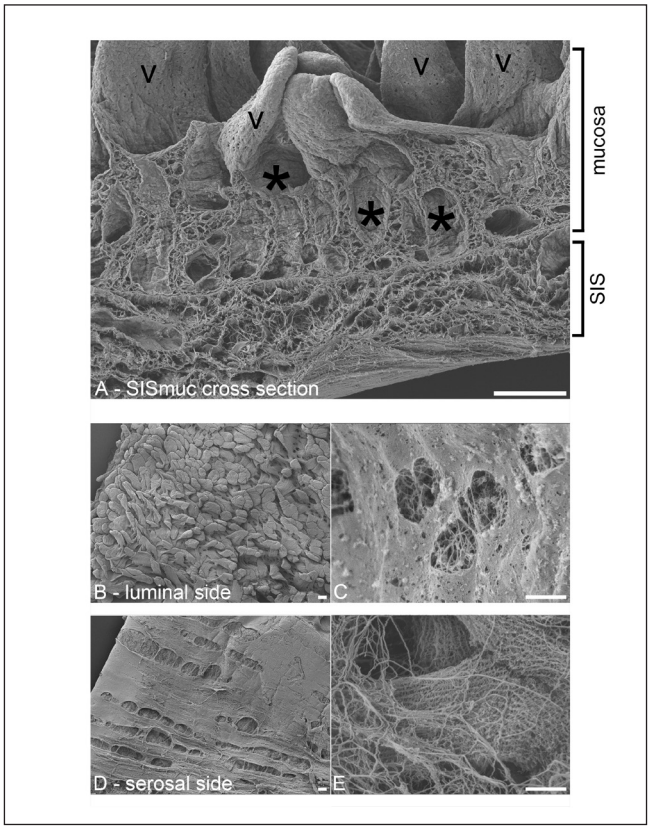


**Fig. 2: The mucosal but not the serosal side of SISmuc matrix shows a complete preserved basal lamina structure after the decellularization process**
(A) Ultrastructural raster electron microscopy analysis of the SISmuc matrix illustrates villi (v) and crypt structures (*), mucosa and small intestinal submucosa (SIS) in a cross section. (B) Top view with low magnification on former mucosa with preserved villi structures covered with a layer of basement membrane (BM), in higher magnification in (C), displaying the presence of small holes with collagen fibers lying underneath. (D) The serosal side of the submucosa consists primarily of fibrillar collagen fibers seen in higher magnification in (E). Scale bars in A, B, D: 100 µm; scale bars in C, E: 1 µm; representative images of n = 1 experiment.

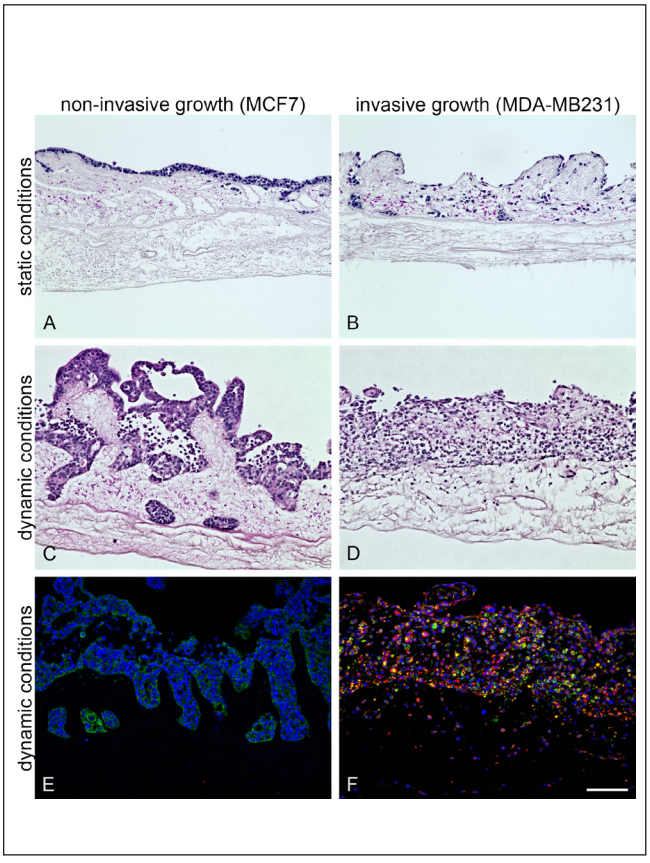


**Fig. 3: Breast cancer cell lines invade the matrix differently**
(A,B) While MCF7 cells (A) grow on top of the scaffold and in some former crypts, MDA-MB-231 cells (B) invade the whole collagen structure when cultured in a static 3D cell culture in cell crowns. (C,D) This effect becomes more pronounced in dynamic cell culture in bioreactors. (A-D) HE-staining of paraffin sections. (E,F) Immunohistochemical staining of pan-cytokeratin (green) and vimentin (red) on paraffin sections reveals the epithelial character of MCF7 cells (E) and the more mesenchymal character of MDA-MB-231 cells (F). Nuclei are stained with DAPI (blue) in E and F. Scale bar in F: 100 µm (same scale for A to F), representative images of n = 3.

in the basal membrane, pores ranging from 1 to 2 µm are visible (Fig. 2C). These pores in the basement membrane have a sharp border and overall rounded shape, suggesting that they are naturally occurring pores rather than damage deriving from the decellularization process. In contrast, the former serosal side of the matrix shows no intact basement membrane structure: Only single collagen fibers can be observed clearly at higher magnification (Fig. 2D,E).

### 3.3 Differentiation between invasive and non-invasive tumor cells

The invasive behavior of cells can be classified by investigating cell growth morphology when seeded on the surface of the SISmuc. Different stages of cancer cell invasion can be mimicked depending on culture condition and cell line. MCF7 breast cancer cells clearly grow on top of the matrix and inside the former crypt structures under static (Fig. 3A) and dynamic culture conditions (Fig. 3C). In contrast, MDA-MB-231 breast cancer cells invade into the whole matrix under static (Fig. 3B) and dynamic culture conditions (Fig. 3D) as shown before (Wallstabe et al., 2019). Immunohistochemical staining of pan-cytokeratin (PCK, green in Fig. 3E,F) and vimentin (Vim, red in Fig. 3E,F) reveals their different epithelial-to-mesenchymal transition (EMT) status. Dynamic conditions promote the invasive character of MDA-MB-231 cells, leading to an increased tumor cell mass within the mucosal part of the SISmuc (Fig. 3D) as well as

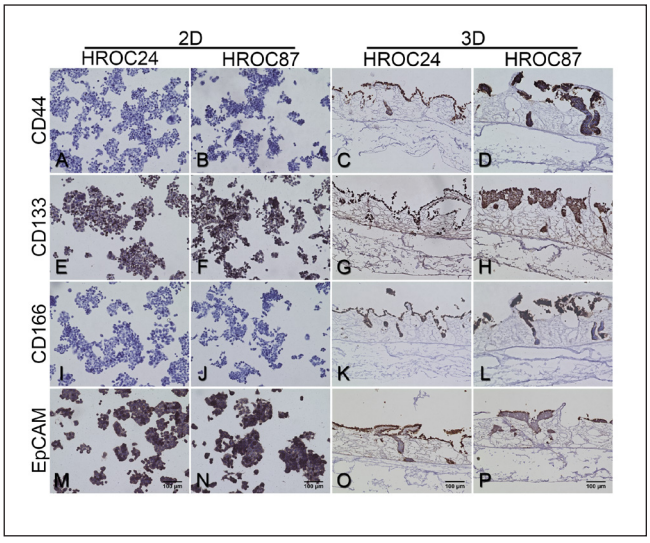


**Fig. 4: 3D cell culture of colorectal cancer (CRC) cells on the SISmuc matrix increases the expression of cancer stem cell (CSC) markers**

Glass slides from 2D and paraffin-embedded sections from 3D cultures were immunohistochemically stained for the stem cell markers CD44 (A to D), CD133 (E to F), CD166 (I to L) und EpCAM (M to P). While the CRC cell lines HROC24 and HROC87 are negative for CD44 (A, B) and CD166 (I, J) under conventional 2D conditions, both cell lines express these markers when cultured on SISmuc (C, D, K, L). Scale bars given in M to P: 100 µm (same scale for A to P), representative images of n = 3.

increased Vim expression (red in Fig. 3F), whereas non-invasive MCF7 cells only show strong PCK expression (green in Fig. 3E).

### 3.4 Enhanced tumor stem cell marker expression under 3D conditions

Cancer stem cells are discussed to present the key subpopulation that should be targeted efficiently for long-term therapeutic success. For CRC model generation, we used two early passage cell lines recently isolated from patients with different tumor stages (HROC24: low grade, HROC87: high grade). HROC24 cells grow mostly as monolayers on top of the matrix and within crypt structures, whereas the more malignant HROC87 form aggregates on top and in former crypt structures of the intestinal matrix. In order to compare stem cell characteristics between 2D and 3D culture conditions, we investigated the expression of the tumor stem cell markers CD44, CD133, CD166 and EpCAM (Willis et al., 2008). In both cell lines, expression of all stem cell markers was only found in 3D conditions, whereas in 2D conditions CD44 and CD166 were not detected in either cell line (Fig. 4).

### 3.5 Differences in gene expression upon targeted therapy under 2D conditions and in 3D tissue models

In previous studies, we have shown an improved correlation of drug responses with clinical observations in 3D lung cancer models based on the tissue matrix technology (Göttlich et al., 2018; Stratmann et al., 2014). In order to reveal involved pathways and biological functions, we now performed microarray-based gene expression analyses of the two lung cancer cell lines A549 and HCC827 in 2D and 3D and compared the respective differences. To adjust for the qualitative difference in RNA isolated from either 2D or 3D culture and to focus on genes relevant for drug response, we compared the ratios of samples treated or untreated with gefitinib, an EGFR tyrosine kinase inhibitor (TKI), under 2D or 3D culture conditions. As HCC827 cells harbor an activating mutation in the *EGFR* gene, while A549 cells do not, only HCC827 were expected to respond to this drug. Gene transcripts with differential expression upon gefitinib treatment in HCC827 but not in A549 cells were selected for further gene ontology (GO) analysis (Tab. 1;

**Tab. 1: Functional overrepresentation analysis of genes showing significant deregulation upon treatment with gefitinib in HCC827 cells not shared with A549 cells[a]**

| | No. of genes changed | Adj. p-value |
|---|---|---|
| **Downregulated in 3D but not in 2D** | | |
| *Cell cycle* | | |
| Cell division | 44 | $1.46 \cdot 10^{-8}$ |
| Cell cycle checkpoint | 15 | $2.64 \cdot 10^{-7}$ |
| Regulation of cell cycle | 33 | $6.33 \cdot 10^{-7}$ |
| G1/S phase transition | 11 | $2.46 \cdot 10^{-5}$ |
| *Metabolic process* | | |
| Canonical glycolysis | 8 | $3.75 \cdot 10^{-8}$ |
| ADP metabolic process | 14 | $1.78 \cdot 10^{-9}$ |
| Pyruvate metabolic process | 15 | $1.81 \cdot 10^{-9}$ |
| *DNA replication* | | |
| Mitotic spindle organization | 9 | $3.33 \cdot 10^{-4}$ |
| Chromosome condensation | 6 | $2.29 \cdot 10^{-3}$ |
| **Upregulated in 3D but not in 2D** | | |
| *Regulation of apoptosis* | | |
| Positive regulation of apoptotic process | 9 | $2.22 \cdot 10^{-3}$ |
| *Cell proliferation* | | |
| Negative regulation of cell proliferation | 9 | $5.72 \cdot 10^{-3}$ |

[a] The table shows selected biological processes and pathways that are deregulated in 3D but not in 2D. Proliferative processes and associated metabolism are down-regulated under 3D conditions. The number of deregulated genes that are involved in each process is shown. Adjusted (multiple testing corrected) p-values are given on the right. Analyses are based on microarray data from 1 experiment in each condition (n = 1).

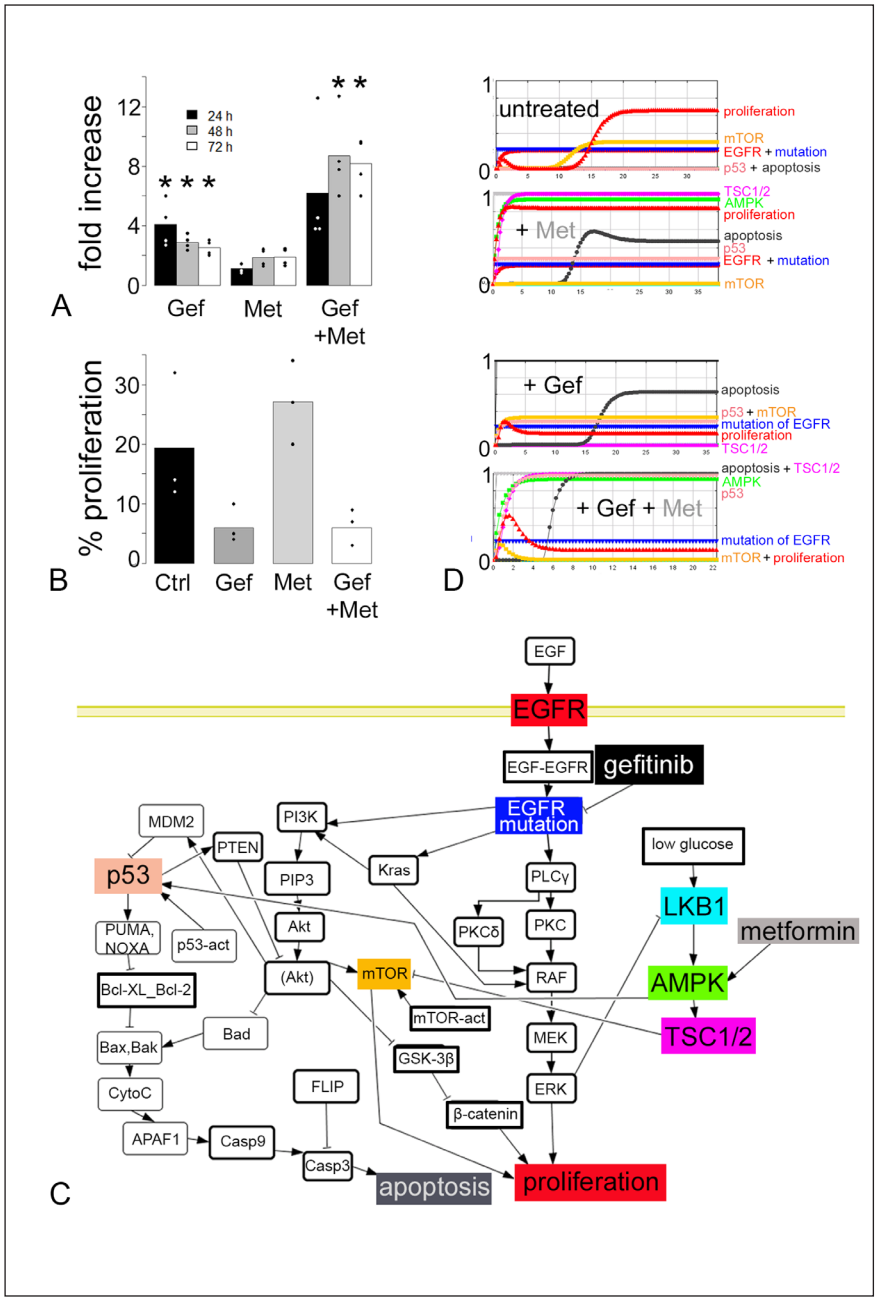


**Fig. 5: Enhanced effects of gefitinib and metformin are predicted and validated by a combined *in silico* and *in vitro* model**

(A) *In vitro*, gefitinib (Gef) and metformin (Met) improve induction of apoptosis in HCC827 cells cultured in 3D. M30 ELISA measurements were performed after 24 h (black bars), 48 h (grey bars) and 72 h (white bars) incubation with either single drugs or the combination (n = 4). (B) Gef alone or Gef + Met decrease proliferation in HCC827 cells (% of Ki-67-positive cells of total cell numbers) compared to the untreated control (Ctrl) (n = 3). (C) An *in silico* topology of HCC827 cells, which harbor an activating mutation of the epidermal growth factor receptor (EGFR) (blue node "mutation of *EGFR*"), was computed in order to simulate treatment responses *in silico*. (D) Simulations by the software SQUAD mirror the response of HCC827 cells to different treatments and reflect *in vitro* results. * in A: $p < 0.05$, Student's t-test. Bars in A and B: mean values, dots in A and B: values of individual experiments (n = 2 for A (2 technical replicates/ experiment) and n = 3 (1 technical replicate/experiment) for B).

pathway enrichment with bubble-plots for pathways upregulated in 3D compared to 2D in Fig. S3[2] and downregulated pathways in Fig. S4[2]).

Gene lists that showed down- and upregulation in 3D models compared to 2D conditions were subjected to an enrichment analysis. A high number of downregulated genes in 3D culture suggests more stringent cell cycle control (cell division, cell cycle checkpoint, G1/S phase transition, cell proliferation), fewer cancer-like metabolic processes (less pronounced expression of pathways such as canonical glycolysis, pyruvate metabolism and ADP metabolism, which are all linked to the Warburg effect) and downregulation of DNA replication (replication initiation, strand elongation, mitotic spindle organization, chromosome condensation). These highly significant observations are in line with the previously observed reduced cell proliferation under 3D conditions. Upregulated genes are, in contrast, linked to positive regulation of apoptotic processes, to the extracellular matrix (ECM) (epithelium development, ECM organization, tissue morphogenesis), to cell differentiation, migration and signal transduction. An increase of tran-

scripts related to inhibition of cell proliferation was observed. All differentially expressed genes with fold-change values are listed in the supplementary file (Tab. S1[3], raw data, and Tab. S2[4], GO-term analysis results).

### 3.6 Simulation module: *in silico* synergistic effect of gefitinib and metformin validated including mutation constellation in 3D tissue lung cancer models

To demonstrate the potential of our 3D model to support exploratory pre-clinical research, bioinformatic simulations were used to discover new targets and promising treatment combinations for CRC and NSCLC (Baur et al., 2019; Göttlich et al., 2018). The work of Göttlich et al. (2018) pointed towards 5' AMP-activated protein kinase (AMPK) activation as a potential treatment strategy for lung cancer. As metformin acts (among other effects) also as an AMPK activator, we tested the combination of gefitinib and metformin on HCC827 cells. In line with our bioinformatic prediction, we observed a significantly increased effect on apoptosis induction for the combination (Fig. 5A). In contrast, proliferation was only affected by gefitinib, but not by metformin, and no enhanced effect on the inhibition of proliferation could be measured for the combination (Fig. 5B).

These data were integrated into a signaling network topology of HCC827 cells (Fig. 5C). We then simulated the dynamics of the signaling network (Fig. 5D). All proteins and their activities change over time, and effector nodes for key cellular responses are calculated in this simulation. The change over time for key cellular responses (proliferation, apoptosis) and central proteins (p53, mTOR, AMPK, etc.) is shown in Figure 5D. This allows an estimation of the cellular responses, for instance enhanced induction of the node "apoptosis" by the combination therapy compared to gefitinib monotherapy, whereas proliferation shows a similar profile in both treatment scenarios (Fig. 5D).

Thus, comparing the pharmacological effects in our *in vitro* 3D cell culture model (Fig. 5A,B) with the *in silico* prediction shows concordant results. The combination of *in vitro* and *in silico* modeling allows to accurately relate the tumor mutation constellation with the most appropriate drug combination. Moreover, as the modular *in vitro* test system as well as the *in silico* simulation module are generic, the approach can be used for testing many other defined drug targets, drugs or drug combinations beyond the example shown in this manuscript.

### 3.7 Modular refinement of the 3D tissue models by adding different cell types of the tumor microenvironment

Further cellular components such as the tumor stroma impact drug responses. Given the strong immunosuppressive effects exerted by the tumor stroma, a targeting of tumor-stroma interactions is of considerable interest. We thus generated models including cell types from the tumor microenvironment such as hECs, immune cells, and fibroblasts. This enables the analysis of new substances and immune therapies. Toxic side effects on non-cancerous cells also can be investigated.

In order to test recently described trispecific hemibodies which target CD45 positive tumor cells in HLA-A2 positive leukemia patients, we seeded HLA-A2 positive hECs on the serosal side of our biological matrix and co-cultured this artificial endothelium with the human HLA-A2 and CD45 dual-positive leukemia cell line THP-1 (Bersi, 2017). In order to assay efficacy and specificity of these hemibodies as an antigen-specific immunotherapeutic approach (Banaszek et al., 2019) in a tissue-like context, we analyzed the induction of apoptosis in THP-1 cells by flow cytometry and compared results from 3D to conventional 2D cell culture. In addition, we compared the efficacy to treatment with the clinically investigated farnesyltransferase inhibitor tipifarnib (Stieglitz et al., 2015). Hemibodies can only recruit T-cells towards dual-positive CD45 and HLA-A2 positive leukemic cells when both antibody parts (AB1 and AB2) bind their respective targets in close proximity. They then assemble to form a functional antibody that also binds to CD3 on T-cells. After addition of HLA-A2-negative PBMCs as effector cells, tumor cell lysis was induced (Fig. 6E,F). Importantly, after 5 days of tipifarnib treatment, we observed the induction of apoptosis in a dose-dependent manner in THP-1 cells in the 3D model and severe damage of the endothelial monolayer confirmed by CD31 staining (Fig. 6D), which, in contrast, was not affected by trispecific hemibody treatment (Fig. 6H). Furthermore, the hemibody treatment yielded a higher efficacy in the 3D model (60% apoptotic THP-1 cells after only 24 hours of treatment compared to 40% apoptotic THP-1 cells in 2D) as shown in Figure 6E and F.

Moreover, the endothelium can be investigated as a barrier for immune cells about to enter the tumor, which is an important issue in immune therapies (Galon et al., 2006). While the endothelial monolayer is shown in green by CD31 staining, tumor cells are stained only with DAPI (Fig. 6I). With the help of flow bioreactors, the diapedesis of immune cells, in this case PBMCs (shown in green), was investigated under dynamic medium flow conditions (Fig. 6J).

Finally, by adding human dermal fibroblasts to different tumor cell lines cultured in our 3D models, we observed different effects on tissue morphology. HCC827 lung tumor cells and A549 cells (Fig. 7A,B in green) showed largely unaltered cell growth patterns compared to monocultured tumor cells. The added fibroblasts simply migrated to deeper matrix areas, while the tumor cells stayed on top of the matrix (Fig. 7C,D in red). Astonishingly, in co-culture with colorectal SW480 cancer cells, non-cancerous fibroblasts induced tumor cell in-

[3] doi:10.14573/altex.2008141s2

[4] doi:10.14573/altex.2008141s3

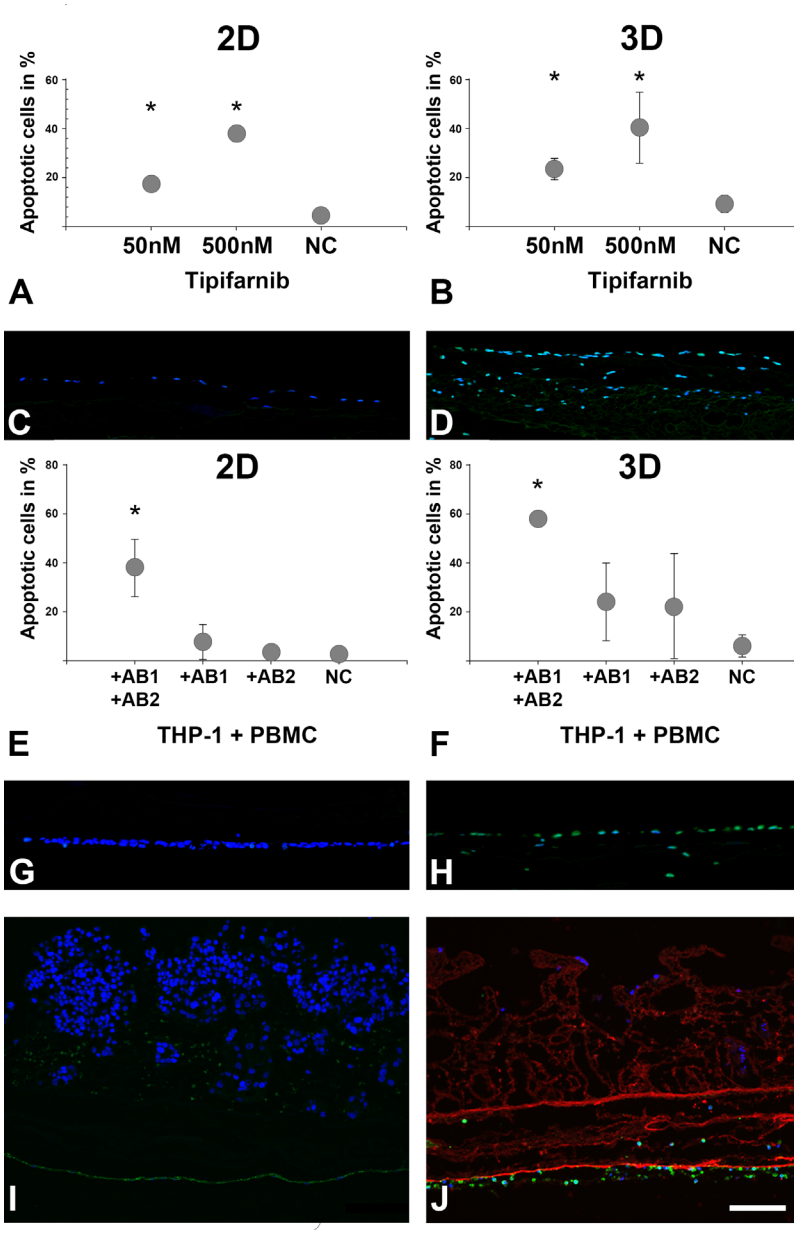


**Fig. 6: Endothelial cells grown on the serosal side of the matrix allow drug efficacy and toxicity testing on THP-1 leukemia cells as well as diapedesis studies with primary immune cells**

(A,B) In flow cytometry analysis of THP-1 cells, the farnesyltransferase inhibitor tipifarnib shows similar induction of apoptosis in conventional 2D cell culture (A) as in the 3D model (B). (C) Untreated DAPI-stained endothelial cells show no DNA damage by TUNEL assay. (D) Tipifarnib-treated (500 nM) cells show a destroyed endothelial layer structure and apoptotic cells (green). (E) In 2D cell culture, the 2 hemibodies, denoted as antibody (AB) 1 and 2, reveal a similar induction of apoptosis in THP-1 cells compared to treatment with 500 nM tipifarnib when given together (A). (F) Increased apoptosis can be seen in the 3D model with no evident damage of the endothelium as demonstrated by TUNEL assay (G). (H) Technical positive control of the TUNEL assay (n = 3, unpaired t-test, Bonferroni corrected). (I) hECs seeded on the former serosal side forming an endothelial layer on the SISmuc. On the mucosal side, the breast cancer cells MCF7 were added. hECs are shown in green in (I) by CD31 staining. (J) A co-culture of hECs with immune cells enables the investigation of immune cell diapedesis as shown in green by CD45 staining. Red in J: Collagen IV is stained as a marker of basal membrane structures within the matrix. Scale bar in I: 100 µm. *, $p < 0.05$ in comparison to negative control (NC). All PBMCs used for the experiments derived from the same donor: n = 4 for 2D and n = 3 for 3D.

vasion into deeper matrix layers, which was accompanied by formation of tumor cell aggregates and by a partial destruction of former crypt structures, indicating the generation of a desmoplastic reaction (Fig. 7E,F). To explore whether this model can be applied for testing of immunotherapies, we added immune cells (PBMCs) and measured the induction of apoptosis in mono- and co-cultures with the allogenic immune cell populations. Under 3D culture conditions, the PBMC-mediated apoptosis in SW480 mono-cultures was reduced in all samples compared to 2D cultures (Fig. 7G), where variation was very high compared to 3D data. The same effects could be seen in SW480 co-cultures with fibroblasts (Fig. S2[2]).

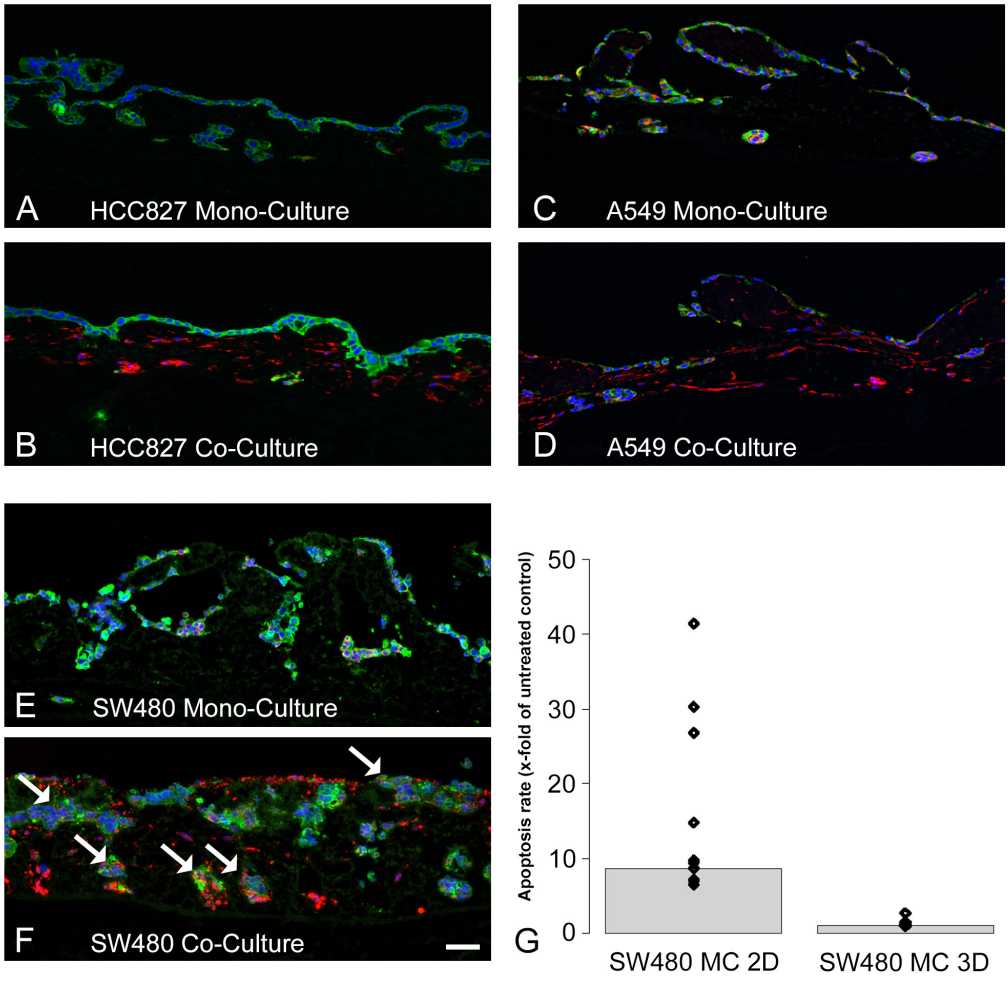


**Fig. 7: The effect of cancer-associated fibroblasts (CAFs) on tumor cell morphology depends on tumor cell type. Compared to 2D culture, 3D conditions reduce allogenic tumor cell killing by immune cells**

(A,B) In HCC827 lung tumor cells (green in A and B), which show a well-differentiated cellular morphology, co-culture (B) with dermal fibroblasts (red in B) has no morphological effect on the growth pattern of these tumor cells. (C,D) Also, in A549 cells (green in C and D), the co-culture with dermal fibroblasts (red in D) does not influence the growth pattern in 3D cell culture. (E,F) In contrast, when highly malignant colorectal SW480 tumor cells (green in E and F) are co-cultured with dermal fibroblasts (red in F), the formation of tumor clusters (white arrows in F) that overgrow former crypt structures is observed (n = 3). G: When allogenic PBMCs were added to SW480 tumor cells, allogenic (and thus largely antigen-independent) tumor cell killing was assessed in order to evaluate the potential usefulness of the models as test systems for MHCI-dependent immune-mediated tumor cell killing. In 2D (n = 6), the apoptosis induction was much higher (with a higher variation) than in 3D (n = 6) in mono- as well as in co-culture with fibroblasts (see Fig. S2[2]). A to F: immunohistochemical staining of PCK (green) and vimentin (Vim). Nuclei are counterstained with DAPI (blue). Scale bar in F: 50 µm for A to F. All PBMCs derived from the same donor: n = 2 (5 technical replicates/experiment) for 2D and n = 3 for 3D.

## 4 Discussion

We report here a modular 3D tissue culture system to generate improved human tumor models with an *in vivo*-like microphysiology. To this aim, we use a decellularized tissue matrix from porcine gut termed SISmuc in which the mucosa is preserved on top of the small intestinal submucosa. In addition, we used for a leukemia tissue model the matrix SISser in which the small intestinal submucosa and the serosa are preserved.

Mina Bissel and others have stressed the huge importance of the microenvironment for physiological cell growth: isolated cells lose their functionality as cues from the microenvironment critically determine the cell fate (Bissell et al., 2003; Bissell, 1981). Advances in 3D technologies, particularly organ-

oids, provide new options in the field of more physiological and personalized models for drug testing and cancer research (Drost and Clevers, 2018; Simian and Bissell, 2017). Nevertheless, organoids have significant disadvantages like their inside-out topology that hinders practical analyses, the very expensive culture conditions due to the need of Matrigel® and growth factors, and high donor variation[5]. Moreover, during organoid formation, dedifferentiation processes are inevitable. Stroma components are often not implemented into the organoids (Baker et al., 2016; Fan et al., 2019) or even get lost (Kim et al., 2019). Immune components can, in contrast, easily be added from peripheral blood (Dijkstra et al., 2018). Animal models such as patient-derived xenografts (PDX) present other challenges: Apart from ethical concerns, they are time-consuming and generally show high variability, which calls for high numbers of animals to achieve statistically meaningful results. While these practical limitations may be overcome, other problems caused by the species barrier are intrinsic to these models. For example, host factors from mice or rats in some cases fail to activate their corresponding receptors on human cells as we have, next to others, demonstrated before (Baur et al., 2019; Francone et al., 2007; Jeffers et al., 1996; Anselmi et al., 2020; Rongvaux et al., 2014).

Decellularized matrices provide complex cues that enhance cell growth, differentiation (Berger et al., 2020) and – as shown here – also stemness potential. The main advantage of our 3D tissue model system compared to organoids is its modular and standardizable set-up with a distinct orientation in a transwell culture plate. Thereby, transmigration of tumor and immune cells across the preserved basement membrane or the added endothelial barrier can be easily evaluated, as the monolayer integrity is visualized by CD31 staining.

To generate *in vitro* models close to the *in vivo* situation suitable for standardization and large-scale production, we use one single pig for the generation of about 150 tumor models out of one single intestine and generate tumor models based on a standardized operating protocol (Göttlich et al., 2016). We utilize the jejunum as in this part one intestinal loop is supplied with blood via one artery and one vein. This enables complete cell removal by thoroughly flushing the vessels with detergent as published before (Jannasch et al., 2015; Linke et al., 2007; Schanz et al., 2010). All investigated cell lines showed a stable proliferation index as well as apoptosis levels between day 11 and about day 18 of a static 3D cell culture, which enables one week of drug testing in a kind of tissue homeostasis. The proliferation index is generally reduced in 3D models in comparison to 2D models, which is more representative of *in vivo* conditions. In investigated cell lines, we find different indices by counting the percentage of Ki-67 positive cells as done in the clinic. Most cell lines range between 20 and 40 percent, which reflects observations from the clinic (Warth et al., 2014; Inwald et al., 2013). Thus, these models should reduce the risk for false-positive results in cytostatic drug testing (Cree et al., 2010).

Further aspects of the models should improve predictivity and mode-of-action analysis: (i) The 3D tissue architecture, its composition of ECM components, and the structure of the basement membrane and bioreactors lead to a more physiological growth of carcinoma cells according to their invasive traits, gene expression/pathway activity (apoptosis, proliferation) and stem cell markers. (ii) Semi-quantitative *in silico* simulations based on these gene expression data allow focused predictions of drug targets and drug combinations. (iii) Addition of cells from the tumor microenvironment enables testing of antigen-specific and MHCI-independent immune therapy and toxicity, and transmigration studies across the endothelium, including assessment of the impact of activated fibroblasts on invasion. Moreover, allogenic immune reactions are reduced in 3D tumor models.

For model generation, tumor cells are seeded on the luminal side – the mucosal side – of the decellularized intestine. Similar to epithelium-derived carcinomas, they are thus physiologically anchored to the basement membrane. We could show by ultrastructural analysis that only on the mucosal, but not on the serosal side, structures of the basement membrane are preserved as a closed layer, showing small, supposedly natural holes at the bottom of the former crypts. These holes are too small for undirected cell migration through them and were proposed to have functions in immune cell trafficking (McClugage and Low, 1984; Takahashi-Iwanaga et al., 1999; Takeuchi and Gonda, 2004). Holes in the basement membrane are also reported in the human bronchus after decellularization (Howat et al., 2002). In our experiments, we observed that the basement membrane represents a strong barrier for tumor cell growth in all investigated cancer entities when the tumor cells are non-invasive. Interestingly, the breast cancer cell line MDA-MB-231, which was formerly described to be highly invasive (Neve et al., 2006), overcomes this barrier and scatters over the whole mucosa in form of single cells as reported before (Wallstabe et al., 2019). In line with hypotheses on EMT and invasion (Zhang and Weinberg, 2018), these MDA-MB-231 cells show a more mesenchymal marker expression, indicating a higher EMT status than the non-invasively growing MCF7 breast cancer cells, as shown here for the first time on our matrix in a 3D tumor model.

### 4.1 Exploiting the modular micro-physiological 3D tissue models for testing immune therapies, fibroblasts and immune cells

Different cell types can also be used to study primary stromal components of tumors. As hECs do not only contribute to the tumor stroma by building a physical barrier but also by secreting soluble signaling molecules, they play an important role when it comes to drug responses in tumor cells (Gubbiotti et al., 2020; Meurette and Mehlen, 2018). Endothelial cells can be seeded on the basolateral side of the matrix to investigate diapedesis of immune cells. For this purpose, specific cell crowns were developed to enable a 3-day upside-down pre-incubation with hECs. These cell crowns can also be manufactured by 3D print-

[5] Lang, S. (2019). What are the pros and cons of using organoids? https://www.drugtargetreview.com/article/48244/what-are-the-pros-and-cons-of-using-organoids/ (accessed 08.12.2020)

ing. Even though no closed basement membrane structure is preserved on this serosal side of the matrix, hECs line up to form a closed endothelium-like structure.

To explore further applications of our model, we also generated a leukemia model in which the acute myeloid leukemia (AML) cell line THP-1 was co-cultured with hECs. As depicted in Figure 6A and B, we could show a dose-dependent efficacy of the drug tipifarnib on top of a 3D endothelium with values similar to 2D. Furthermore, tipifarnib treatment resulted in side effects indicated by damage to the endothelium. In clinical studies, tipifarnib did not succeed in AML therapy (Thomas and Elhamri, 2007).

We could observe a higher efficacy and specificity in our leukemia 3D model when we tested trispecific antibodies (Banaszek et al., 2019) as an expansion of the bispecific T-cell engaging (BiTE) therapy concept (Goebeler and Bargou, 2020). Here, the CD3-binding site of a split trispecific antibody, referred to as a hemibody, is reconstituted after binding to another hemibody. For reconstitution, both hemibodies have to bind specifically to an antigen expressed on leukemic tumor cells (CD45, marker of hematopoietic cells) and to an antigen expressed in all nucleated cells of the patient (HLA-A2). Thereby HLA-A2-negative but CD45-positive immune cell populations from donors and HLA-A2-positive but CD45-negative patient cells as hECs should not be affected. Accordingly, we could not observe toxic effects in only HLA-A2-positive endothelial cells, demonstrating next to its efficacy also the specificity of this immunotherapeutic strategy. This has allowed us to show that our models are suitable to test and explore antigen-specific but MHCI-independent immune therapies *in vitro*. In contrast to other frequently used endothelial 3D cell culture models, like transwell plates, our model allows direct and close contact of hECs to the ECM. This is important as ECM cues change signaling in endothelial cells (Fukuhara et al., 2009). Furthermore, integrating the endothelium in our model enables us to study the transmigration of immune cells over the endothelial barrier. This is an important feature for the improvement of immune therapies, as the presence of immune cells within the tumor is currently the best predictor for a treatment response to immune checkpoint inhibition (Lu et al., 2019; Tumeh et al., 2014).

Fibroblasts are another major part of the tumor stroma, contributing to physical and immunological barriers (Kalluri, 2016). These stromal cells can also be included in the 3D models. Notably, with or without tumor cells, fibroblasts cross the basement membrane of our matrix and grow inside the whole matrix. Their relevance to tumor tissue morphology is demonstrated in our 3D CRC model, where SW480 CRC cells show signs of collective invasion in co-cultures with primary dermal fibroblasts (Nietzer et al., 2016). This results in the destruction of former crypt structures in the SISmuc (Nietzer et al., 2016). The role of fibroblasts in tumor metastasis has also been confirmed in animal models (Gao et al., 2019), and they are important determinants of cancer therapy (Valkenburg et al., 2018). Our new and refined *in vitro* models thus reflect the behavior of non-invasive tumor cells as well as single cell invasion, but also collective invasion supported by the tumor stroma. This provides new options for drug testing in different tissue-like contexts. For example, it can be tested if substances interfere with the interaction of tumor cells with surrounding stroma cells and can thereby hinder tumor cell invasion.

An adjustment of *in vitro* to patient conditions is, for instance, suggested by the fact that our 3D model – similar to patients – does not imply a correlation between HSP90 inhibitor efficacy and a KRAS mutation in lung tumors (Göttlich et al., 2018). While such correlation had been suggested by 2D and animal models (Sos et al., 2009), clinical studies revealed this to be most likely an artifact (Socinski et al., 2013).

### 4.2 In which aspects are modular 3D tissue models an improvement?

To analyze differences between tumor cells cultured in 2D versus 3D in more detail, we first looked at stemness. CD44 functions as a receptor that binds to hyaluronic acid and other components of the ECM (Nusgens, 2010). It is widely recognized as a stem cell marker in solid tumors, acts as a co-receptor and regulates cell behavior by integrating external signals (Wang et al., 2018). Other markers expressed by healthy stem cells, such as, e.g., CD133, also are found on cancer stem cells (CSC) (Sahlberg et al., 2014; Wang et al., 2012). EpCAM is important for epithelial cell-to-cell contacts but also has oncogenic potential in cell signaling by releasing its intracellular domain (Munz et al., 2009). Together with CD44, EpCAM significantly affects the clinical course in CRC (Liu et al., 2014). CD166, which is found in the intestinal stem cell niche, also is discussed as a cancer stem cell marker (Levin et al., 2010). Staining of these markers revealed a higher expression of all investigated markers under 3D conditions compared to 2D conditions. As tumor cells can acquire mesenchymal features and stem cell characteristics during invasion and development of resistance (Shibue and Weinberg, 2017), it remains open whether CSCs are more likely than non-CSCs to grow on the OncoVaSc-TERM® scaffold or whether stem cell features develop in non-CSCs due to the 3D culture conditions. Still, considering that the postulated CSC population comprises the cells that are most likely to escape from conventional cytostatic chemotherapy or radiotherapy, their targeting is thought to be essential for long-lasting therapeutic success (Shibue and Weinberg, 2017). The enhanced stemness of tumor cells cultured on the matrix in 3D may explain their generally higher chemoresistance compared to 2D cultured cells, which should be advantageous for the identification of efficient drugs for cancer therapy. Nevertheless, inhibitors that are well known to work in the clinic, such as gefitinib, do reliable work in our 3D tissue test systems (Stratmann et al., 2014; Göttlich et al., 2018). To determine more general differences between 2D and 3D expression in molecular detail, we compared the ratio of treated to non-treated gefitinib-responsive and non-responsive tumor cells carrying an EGFR biomarker or not. Gene ontology (GO) enrichment analysis of microarrays of 2D- and 3D-cultured cells normalized to untreated cells of the respective culture condition reveals highly significant differ-

ences in gene clusters for proliferation, cell cycle and apoptosis. Given the more physiological environment and growth pattern of 3D cell culture, there is reason to believe that our 3D models reflect clinical responses more accurately than conventional 2D models.

To understand the systems biology of targeted treatments as applied in the clinic and to connect our *in vivo*-like 3D models to the *in silico* prediction module, we integrated further analysis parameters going beyond viability, such as proliferation, apoptosis and signaling (Stratmann et al., 2014). Thus, central signaling cascades, known from literature and databases, are set up *in silico* with the software CellDesigner as a topology to reflect interdependencies by feedback loops and redundancies. The interconnectivity of the network that includes parameters such as kinase cascades, mutations, *in vitro* measured drug responses of proliferation, apoptosis, and EMT, subsequently provides a basis for optimized simulations of drug effects. The *in silico* module starts from a Boolean decision network, which then is dynamically simulated and investigated by the software SQUAD using differential equations (Di Cara et al., 2007). This enables approximations of systemic drug responses even without detailed kinetic information. As a generic example, we tested the effects of the AMPK activator metformin on HCC827 cells, as AMPK activation was predicted to be a promising target before (Göttlich et al., 2018). Metformin is discussed to reduce the risk to die from cancer in diabetic patients (Chae et al., 2016; Sun et al., 2015). Increased apoptosis induction by metformin and the EGFR inhibitor gefitinib was predicted *in silico* and demonstrated *in vitro*. Starting from these experimental observations and combined with *in silico* modeling, hypotheses can be generated for mode-of-actions that are exemplified in the following: Looking at the topology, the induction of proliferation by metformin monotherapy could be explained systemically by cellular pathway switching: Upon mTOR inhibition, a compensatory activation of the MEK-ERK pathway is likely to occur. Though there is no direct connection between these pathways, the cellular system change is instead mediated by a concerted reaction of the complete network (connection via PI3K-AKT, and both drugs have an enhancing effect via p53 on apoptosis). However, this MEK-ERK pathway activation could then be targeted by the combination with gefitinib. Hence, there is no direct interaction between the pathways. Instead, a whole system state switch occurs, which would have been difficult to hypothesize by just looking at the data obtained from our 3D culture system. Thus, "wet lab" research performed in this culture system can benefit from additional *in silico* modeling. *Vice versa*, *in silico* modeling can only be as good as the data the algorithms are fed with. While integrated mutational signatures cannot yet predict the response to a treatment, *in silico* analyses can identify promising candidates that can then be pretested in our 3D tumor tissue models. This could strongly reduce the number of animals required to develop combination therapies, as only the most promising combinations would have to be tested in animals. In addition, testing of individually tailored therapies could be greatly accelerated, which may become critical for precision medicine in oncology.

Finally, we show that a 3D CRC model with or without fibroblasts is much more resistant towards induction of apoptosis by allogenic PBMCs than a 2D model. This represents a first step towards establishing immunotherapeutic 3D test systems with material from different donors. Thus, the model provides a good starting point for testing MHCI-dependent immunotherapeutics such as immune checkpoint-inhibitors. In addition to antigen-specific T-cell engaging testing, we have already demonstrated that our 3D tumor models can be used to test CAR T-cell efficacy in solid tumors as a further antigen-specific approach and to develop new engineering strategies (Stuber et al., 2020; Wallstabe et al., 2019).

To summarize, benefits of our platform include a reduction of animal experiments, improved screening modalities for anticancer drug development, the possibility to include immune cells and stromal components, and hence a more reliable testing of immune therapies. We are thus confident that our modular and standardizable test platform, which closely mimics cellular *in vivo* conditions, has a high potential for basic and applied research.

## References


Albritton, J. L. and Miller, J. S. (2017). 3D bioprinting: Improving in vitro models of metastasis with heterogeneous tumor microenvironments. *Dis Model Mech 10*, 3-14. doi:10.1242/dmm.025049

Anselmi, G., Vaivode, K., Dutertre, C. A. et al. (2020). Engineered niches support the development of human dendritic cells in humanized mice. *Nat Commun 11*, 2054. doi:10.1038/s41467-020-15937-y

Arrowsmith, J. and Miller, P. (2013). Trial watch: Phase II and phase III attrition rates 2011-2012. *Nat Rev Drug Discov 12*, 569. doi:10.1038/nrd4090

Baker, L. A., Tiriac, H., Clevers, H. et al. (2016). Modeling pancreatic cancer with organoids. *Trends Cancer 2*, 176-190. doi:10.1016/j.trecan.2016.03.004

Banaszek, A., Bumm, T. G. P., Nowotny, B. et al. (2019). On-target restoration of a split T cell-engaging antibody for precision immunotherapy. *Nat Commun 10*, 5387. doi:10.1038/s41467-019-13196-0

Baur, F., Nietzer, S. L., Kunz, M. et al. (2019). Connecting cancer pathways to tumor engines: A stratification tool for colorectal cancer combining human in vitro tissue models with Boolean in silico models. *Cancers (Basel) 12*, doi:10.3390/cancers12010028

Berger, C., Bjorlykke, Y., Hahn, L. et al. (2020). Matrix decoded – A pancreatic extracellular matrix with organ specific cues guiding human iPSC differentiation. *Biomaterials 244*, 119766. doi:10.1016/j.biomaterials.2020.119766

Bersi, H. (2017). Etablierung eines 3D in vitro Blutgefäß-/Gewebemodells zur Testung spezifischer Therapeutika zur Leukämiebehandlung (Establishment of a 3D in vitro blood vessel / tissue model to test specific therapeutic agents to treat leukemia). University of Wuerzburg, medical faculty, urn:nbn:de:bvb:20-opus-152506.

Bhattacharjee, Y. (2012). Biomedicine. Pharma firms push for sharing of cancer trial data. *Science 338*, 29. doi:10.1126/science.338.6103.29

Bissell, M. J. (1981). The differentiated state of normal and malignant cells or how to define a "normal" cell in culture. *Int Rev Cytol 70*, 27-100. doi:10.1016/s0074-7696(08)61130-4

Bissell, M. J., Rizki, A. and Mian, I. S. (2003). Tissue architecture: The ultimate regulator of breast epithelial function. *Curr Opin Cell Biol 15*, 753-762. doi:10.1016/j.ceb.2003.10.016

Chae, Y. K., Arya, A., Malecek, M. K. et al. (2016). Repurposing metformin for cancer treatment: Current clinical studies. *Oncotarget 7*, 40767-40780. doi:10.18632/oncotarget.8194

Cree, I. A., Glaysher, S. and Harvey, A. L. (2010). Efficacy of anti-cancer agents in cell lines versus human primary tumour tissue. *Curr Opin Pharmacol 10*, 375-379. doi:10.1016/j.coph.2010.05.001

Di Cara, A., Garg, A., De Micheli, G. et al. (2007). Dynamic simulation of regulatory networks using squad. *BMC Bioinformatics 8*, 462. doi:10.1186/1471-2105-8-462

Dijkstra, K. K., Cattaneo, C. M., Weeber, F. et al. (2018). Generation of tumor-reactive T cells by co-culture of peripheral blood lymphocytes and tumor organoids. *Cell 174*, 1586-1598.e12. doi:10.1016/j.cell.2018.07.009

Drost, J. and Clevers, H. (2018). Organoids in cancer research. *Nat Rev Cancer 18*, 407-418. doi:10.1038/s41568-018-0007-6

EC - European Commission (2020). 2019 report on the statistics on the use of animals for scientific purposes in the Member States of the European Union in 2015-2017. Brussels, 5.2.2020

Fan, H., Demirci, U. and Chen, P. (2019). Emerging organoid models: Leaping forward in cancer research. *J Hematol Oncol 12*, 142. doi:10.1186/s13045-019-0832-4

Francone, T. D., Landmann, R. G., Chen, C. T. et al. (2007). Novel xenograft model expressing human hepatocyte growth factor shows ligand-dependent growth of c-Met-expressing tumors. *Mol Cancer Ther 6*, 1460-1466. doi:10.1158/1535-7163.MCT-06-0466

Fuchs, M., Kreutzer, F. P., Kapsner, L. A. et al. (2020). Integrative bioinformatic analyses of global transcriptome data decipher novel molecular insights into cardiac anti-fibrotic therapies. *Int J Mol Sci 21*, 4727. doi:10.3390/ijms21134727

Fukuhara, S., Sako, K., Noda, K. et al. (2009). Tie2 is tied at the cell-cell contacts and to extracellular matrix by angiopoietin-1. *Exp Mol Med 41*, 133-139. doi:10.3858/emm.2009.41.3.016

Galon, J., Costes, A., Sanchez-Cabo, F. et al. (2006). Type, density, and location of immune cells within human colorectal tumors predict clinical outcome. *Science 313*, 1960-1964. doi:10.1126/science.1129139

Gao, Q., Yang, Z., Xu, S. et al. (2019). Heterotypic CAF-tumor spheroids promote early peritoneal metastatis of ovarian cancer. *J Exp Med 216,* 688-703. doi:10.1084/jem.20180765

Goebeler, M. E. and Bargou, R. C. (2020). T cell-engaging therapies – Bites and beyond. *Nat Rev Clin Oncol 17*, 418-434. doi:10.1038/s41571-020-0347-5

Göttlich, C., Muller, L. C., Kunz, M. et al. (2016). A combined 3D tissue engineered in vitro/in silico lung tumor model for predicting drug effectiveness in specific mutational backgrounds. *J Vis Exp*, e53885. doi:10.3791/53885

Göttlich, C., Kunz, M., Zapp, C. et al. (2018). A combined tissue-engineered/in silico signature tool patient stratification in lung cancer. *Mol Oncol 12*, 1264-1285. doi:10.1002/1878-0261.12323

Groeber, F., Engelhardt, L., Lange, J. et al. (2016). A first vascularized skin equivalent as an alternative to animal experimentation. *ALTEX 33*, 415-422. doi:10.14573/altex.1604041

Gubbiotti, M. A., Buraschi, S., Kapoor, A. et al. (2020). Proteoglycan signaling in tumor angiogenesis and endothelial cell autophagy. *Semin Cancer Biol 62*, 1-8. doi:10.1016/j.semcancer.2019.05.003

Howat, W. J., Barabas, T., Holmes, J. A. et al. (2002). Distribution of basement membrane pores in bronchus revealed by microscopy following epithelial removal. *J Struct Biol 139*, 137-145. doi:10.1016/s1047-8477(02)00589-0

Inwald, E. C., Klinkhammer-Schalke, M., Hofstadter, F. et al. (2013). Ki-67 is a prognostic parameter in breast cancer patients: Results of a large population-based cohort of a cancer registry. *Breast Cancer Res Treat 139*, 539-552. doi:10.1007/s10549-013-2560-8

Jannasch, M., Groeber, F., Brattig, N. W. et al. (2015). Development and application of three-dimensional skin equivalents for the investigation of percutaneous worm invasion. *Exp Parasitol 150*, 22-30. doi:10.1016/j.exppara.2015.01.005

Jeffers, M., Rong, S. and Vande Woude, G. F. (1996). Hepatocyte growth factor/scatter factor-met signaling in tumorigenicity and invasion/metastasis. *J Mol Med (Berl) 74*, 505-513. doi:10.1007/BF00204976

Kalluri, R. (2016). The biology and function of fibroblasts in cancer. *Nat Rev Cancer 16*, 582-598. doi:10.1038/nrc.2016.73

Katt, M. E., Placone, A. L., Wong, A. D. et al. (2016). In vitro tumor models: Advantages, disadvantages, variables, and selecting the right platform. *Front Bioeng Biotechnol 4*, 12. doi:10.3389/fbioe.2016.00012

Kim, M., Mun, H., Sung, C. O. et al. (2019). Patient-derived lung cancer organoids as in vitro cancer models for therapeutic screening. *Nat Commun 10*, 3991. doi:10.1038/s41467-019-11867-6

Levin, T. G., Powell, A. E., Davies, P. S. et al. (2010). Characterization of the intestinal cancer stem cell marker CD166 in the human and mouse gastrointestinal tract. *Gastroenterology 139*, 2072-2082.e5. doi:10.1053/j.gastro.2010.08.053

Linke, K., Schanz, J., Hansmann, J. et al. (2007). Engineered liver-like tissue on a capillarized matrix for applied research. *Tissue Eng 13*, 2699-2707. doi:10.1089/ten.2006.0388

Liu, D., Sun, J., Zhu, J. et al. (2014). Expression and clinical significance of colorectal cancer stem cell marker $EpCAM^{high}/CD44^{+}$ in colorectal cancer. *Oncol Lett 7*, 1544-1548. doi:10.3892/ol.2014.1907

Lu, S., Wang, H. and Taube, J. M. (2019). Different biomarker modalities and response to anti-PD-1/PD-L1 therapies-reply. *JAMA Oncol.* doi:10.1001/jamaoncol.2019.5154

Matsuoka, Y., Funahashi, A., Ghosh, S. et al. (2014). Modeling

and simulation using celldesigner. *Methods Mol Biol 1164*, 121-145. doi:10.1007/978-1-4939-0805-9_11

McClugage, S. G. and Low, F. N. (1984). Microdissection by ultrasonication: Porosity of the intestinal epithelial basal lamina. *Am J Anat 171*, 207-216. doi:10.1002/aja.1001710206

Meurette, O. and Mehlen, P. (2018). Notch signaling in the tumor microenvironment. *Cancer Cell 34*, 536-548. doi:10.1016/j.ccell.2018.07.009

Mullins, C. S., Micheel, B., Matschos, S. et al. (2019). Integrated biobanking and tumor model establishment of human colorectal carcinoma provides excellent tools for preclinical research. *Cancers (Basel) 11*, 1520. doi:10.3390/cancers11101520

Munz, M., Baeuerle, P. A. and Gires, O. (2009). The emerging role of EpCAM in cancer and stem cell signaling. *Cancer Res 69,* 5627-5629. doi:10.1158/0008-5472.CAN-09-0654

Nath, S. and Devi, G. R. (2016). Three-dimensional culture systems in cancer research: Focus on tumor spheroid model. *Pharmacol Ther 163*, 94-108. doi:10.1016/j.pharmthera.2016.03.013

Neve, R. M., Chin, K., Fridlyand, J. et al. (2006). A collection of breast cancer cell lines for the study of functionally distinct cancer subtypes. *Cancer Cell 10*, 515-527. doi:10.1016/j.ccr.2006.10.008

Nietzer, S., Baur, F., Sieber, S. et al. (2016). Mimicking metastases including tumor stroma: A new technique to generate a three-dimensional colorectal cancer model based on a biological decellularized intestinal scaffold. *Tissue Eng Part C Methods 22*, 621-635. doi:10.1089/ten.TEC.2015.0557

Nusgens, B. V. (2010). Hyaluronic acid and extracellular matrix: A primitive molecule? [Article in French]. *Ann Dermatol Venereol 137*, *Suppl 1*, S3-8. doi:10.1016/S01519638(10)70002-8

Raudvere, U., Kolberg, L., Kuzmin, I. et al. (2019). g:Profiler: A web server for functional enrichment analysis and conversions of gene lists (2019 update). *Nucleic Acids Res 47*, W191-W198. doi:10.1093/nar/gkz369

Rongvaux, A., Takizawa, H., Strowig, T. et al. (2013). Human hemato-lymphoid system mice: Current use and future potential for medicine. *Annu Rev Immunol 31*, 635-674. doi:10.1146/annurev-immunol-032712-095921

Rongvaux, A., Willinger, T., Martinek, J. et al. (2014). Development and function of human innate immune cells in a humanized mouse model. *Nat Biotechnol 32*, 364-372. doi:10.1038/nbt.2858

Sahlberg, S. H., Spiegelberg, D., Glimelius, B. et al. (2014). Evaluation of cancer stem cell markers CD133, CD44, CD24: Association with AKT isoforms and radiation resistance in colon cancer cells. *PLoS One 9*, e94621. doi:10.1371/journal.pone.0094621

Santo, V. E., Rebelo, S. P., Estrada, M. F. et al. (2017). Drug screening in 3D in vitro tumor models: Overcoming current pitfalls of efficacy read-outs. *Biotechnol J 12*. doi:10.1002/biot.201600505

Schanz, J., Pusch, J., Hansmann, J. et al. (2010). Vascularised human tissue models: A new approach for the refinement of biomedical research. *J Biotechnol 148*, 56-63. doi:10.1016/j.jbiotec.2010.03.015

Schweinlin, M., Rossi, A., Lodes, N. et al. (2017). Human barrier models for the in vitro assessment of drug delivery. *Drug Deliv Transl Res 7*, 217-227. doi:10.1007/s13346-016-0316-9

Shibue, T. and Weinberg, R. A. (2017). EMT, CSCs, and drug resistance: The mechanistic link and clinical implications. *Nat Rev Clin Oncol 14*, 611-629. doi:10.1038/nrclinonc.2017.44

Simian, M. and Bissell, M. J. (2017). Organoids: A historical perspective of thinking in three dimensions. *J Cell Biol 216*, 31-40. doi:10.1083/jcb.201610056

Socinski, M. A., Goldman, J., El-Hariry, I. et al. (2013). A multicenter phase II study of ganetespib monotherapy in patients with genotypically defined advanced non-small cell lung cancer. *Clin Cancer Res 19*, 3068-3077. doi:10.1158/1078-0432.CCR-12-3381

Song, Y., Rongvaux, A., Taylor, A. et al. (2019). A highly efficient and faithful MDS patient-derived xenotransplantation model for pre-clinical studies. *Nat Commun 10*, 366. doi:10.1038/s41467-018-08166-x

Sos, M. L., Michel, K., Zander, T. et al. (2009). Predicting drug susceptibility of non-small cell lung cancers based on genetic lesions. *J Clin Invest 119*, 1727-1740. doi:10.1172/JCI37127

Stieglitz, E., Ward, A. F., Gerbing, R. B. et al. (2015). Phase II/III trial of a pre-transplant farnesyl transferase inhibitor in juvenile myelomonocytic leukemia: A report from the children's oncology group. *Pediatr Blood Cancer 62*, 629-636. doi:10.1002/pbc.25342

Stratmann, A. T., Fecher, D., Wangorsch, G. et al. (2014). Establishment of a human 3D lung cancer model based on a biological tissue matrix combined with a Boolean in silico model. *Mol Oncol 8*, 351-365. doi:10.1016/j.molonc.2013.11.009

Stuber, T., Monjezi, R., Wallstabe, L. et al. (2020). Inhibition of TGF-beta-receptor signaling augments the antitumor function of ROR1-specific CAR T-cells against triple-negative breast cancer. *J Immunother Cancer 8*, e000676. doi:10.1136/jitc-2020-000676

Sun, J., Zhao, M., Jia, P. et al. (2015). Deciphering signaling pathway networks to understand the molecular mechanisms of metformin action. *PLoS Comput Biol 11*, e1004202. doi:10.1371/journal.pcbi.1004202

Takahashi-Iwanaga, H., Iwanaga, T. and Isayama, H. (1999). Porosity of the epithelial basement membrane as an indicator of macrophage-enterocyte interaction in the intestinal mucosa. *Arch Histol Cytol 62*, 471-481. doi:10.1679/aohc.62.471

Takeuchi, T. and Gonda, T. (2004). Distribution of the pores of epithelial basement membrane in the rat small intestine. *J Vet Med Sci 66*, 695-700. doi:10.1292/jvms.66.695

Thomas, X. and Elhamri, M. (2007). Tipifarnib in the treatment of acute myeloid leukemia. *Biologics 1*, 415-424.

Tumeh, P. C., Harview, C. L., Yearley, J. H. et al. (2014). PD-1 blockade induces responses by inhibiting adaptive immune resistance. *Nature 515*, 568-571. doi:10.1038/nature13954

Valkenburg, K. C., de Groot, A. E. and Pienta, K. J. (2018). Targeting the tumour stroma to improve cancer therapy. *Nat Rev*

*Clin Oncol 15*, 366-381. doi:10.1038/s41571-018-0007-1
van Duinen, V., Trietsch, S. J., Joore, J. et al. (2015). Microfluidic 3D cell culture: From tools to tissue models. *Curr Opin Biotechnol 35*, 118-126. doi:10.1016/j.copbio.2015.05.002
Wallstabe, L., Göttlich, C., Nelke, L. C. et al. (2019). ROR1-car T cells are effective against lung and breast cancer in advanced microphysiologic 3D tumor models. *JCI Insight 4*, e126345. doi:10.1172/jci.insight.126345
Walsh, N. C., Kenney, L. L., Jangalwe, S. et al. (2017). Humanized mouse models of clinical disease. *Annu Rev Pathol 12*, 187-215. doi:10.1146/annurev-pathol-052016-100332
Wang, C., Xie, J., Guo, J. et al. (2012). Evaluation of CD44 and CD133 as cancer stem cell markers for colorectal cancer. *Oncol Rep 28*, 1301-1308. doi:10.3892/or.2012.1951
Wang, L., Zuo, X., Xie, K. et al. (2018). The role of CD44 and cancer stem cells. *Methods Mol Biol 1692*, 31-42. doi:10.1007/978-1-4939-7401-6_3
Warth, A., Cortis, J., Soltermann, A. et al. (2014). Tumour cell proliferation (Ki-67) in non-small cell lung cancer: A critical reappraisal of its prognostic role. *Br J Cancer 111*, 1222-1229. doi:10.1038/bjc.2014.402
Weeber, F., Ooft, S. N., Dijkstra, K. K. et al. (2017). Tumor organoids as a pre-clinical cancer model for drug discovery. *Cell Chem Biol 24*, 1092-1100. doi:10.1016/j.chembiol.2017.06.012
Wickham, H. (2009). *ggplot2 – Elegant Graphics for Data Analysis*. Germany: Springer.
Willis, N. D., Przyborski, S. A., Hutchison, C. J. et al. (2008). Colonic and colorectal cancer stem cells: Progress in the search for putative biomarkers. *J Anat 213*, 59-65. doi:10.1111/j.1469-7580.2008.00917.x
Xu, X., Farach-Carson, M. C. and Jia, X. (2014). Three-dimensional in vitro tumor models for cancer research and drug evaluation. *Biotechnol Adv 32*, 1256-1268. doi:10.1016/j.biotechadv.2014.07.009
Yada, E., Wada, S., Yoshida, S. et al. (2018). Use of patient-derived xenograft mouse models in cancer research and treatment. *Future Sci OA 4*, FSO271. doi:10.4155/fsoa-2017-0136
Zhang, Y. and Weinberg, R. A. (2018). Epithelial-to-mesenchymal transition in cancer: Complexity and opportunities. *Front Med 12*, 361-373. doi:10.1007/s11684-018-0656-6

## Conflict of interest

The authors declare that they have no conflicts of interest.

## Author contributions

JK, FS, HL, MS, LN, TS, FB, CG, MP, CB, CK, JW, MP, HW: cell culture experiments, methods and tests; MK, MF, TD: bioinformatics and simulations; all authors were involved in data analysis; GD, TD, SN: supervision, led and guided the study; GD, TD, SN: manuscript draft. All authors read and corrected the manuscript and agreed to the final version.

## Acknowledgements

We are grateful for support from the BMBF in the call "Alternative methods to animal experiments" (GD, TD, project: 031L0129A/B; all parts concerning animal reduction strategies) as well as in the project 031L0262C (MK), the IZKF Würzburg (GD, JK: Project: B354; parts on coculture with stroma), as well as Claus-Jürgen Scholz and colleagues from the Core Unit Systems Medicine of the IZKF Würzburg, the Bayern Fit program (LN, FB, SLN) and the Bavarian Research Foundation (GD, TD, JW: project: AZ-1365-18; parts on transmigration of immune cells, and their signaling). For providing HROC24 and HROC87 early passage cells, we thank Michael Linnebacher. Furthermore, we would like to thank Heide Häfner for technical assistance in the lab, Christian Stigloher, Claudia Gehrig and Daniela Bunsen for their support in ultrastructural analysis and G. Stuhler for supply of PBMCs and trispecific antibodies. This publication was supported by the Open Access Publication Fund of the University of Würzburg.